



Pushing the boundaries
of chemistry?
It takes
#HumanChemistry

Make your curiosity and talent as a chemist matter to the world with a specialty chemicals leader. Together, we combine cutting-edge science with engineering expertise to create solutions that answer real-world problems. Find out how our approach to technology creates more opportunities for growth, and see what chemistry can do for you at:

[evonik.com/career](https://www.evonik.com/career)



Nanoimprint Lithography Facilitated Plasmonic-Photonic Coupling for Enhanced Photoconductivity and Photocatalysis

Vaibhav Gupta, Swagato Sarkar, Olha Aftenieva, Takuya Tsuda, Labeesh Kumar, Daniel Schletz, Johannes Schultz, Anton Kiriya, Andreas Fery, Nicolas Vogel, and Tobias A. F. König*


Imprint lithography has emerged as a reliable, reproducible, and rapid method for patterning colloidal nanostructures. As a promising alternative to top-down lithographic approaches, the fabrication of nanodevices has thus become effective and straightforward. In this study, a fusion of interference lithography (IL) and nanosphere imprint lithography on various target substrates ranging from carbon film on transmission electron microscope grid to inorganic and dopable polymer semiconductor is reported. 1D plasmonic photonic crystals are printed with 75% yield on the centimeter scale using colloidal ink and an IL-produced polydimethylsiloxane stamp. Atomically smooth facet, single-crystalline, and monodisperse colloidal building blocks of gold (Au) nanoparticles are used to print 1D plasmonic grating on top of a titanium dioxide (TiO₂) slab waveguide, producing waveguide-plasmon polariton modes with superior 10 nm spectral line-width. Plasmon-induced hot electrons are confirmed via two-terminal current measurements with increased photoresponsivity under guiding conditions. The fabricated hybrid structure with Au/TiO₂ heterojunction enhances photocatalytic processes like degradation of methyl orange (MO) dye molecules using the generated hot electrons. This simple colloidal printing technique demonstrated on silicon, glass, Au film, and naphthalenediimide polymer thus marks an important milestone for large-scale implementation in optoelectronic devices.

1. Introduction

Metal nanoparticles (NPs) are the vital constituents of nanotechnology. The interaction of NPs with light leads to striking electrical, optical magnetic properties with a plethora of applications.^[1,2] Plasmonic NPs can trap the light into subwavelength volumes in the form of localized surface plasmon; this enhanced mode volume is important for photochemistry,^[3] photophysics,^[4] biosensing,^[5] photocatalysis,^[6] photonic devices,^[7] plasmon-enhanced chirality,^[8,9] nonlinear physics,^[10] and so on. However, mitigating the Ohmic losses due to the high scattering rate of electrons and assembling the plasmonic building block with cost-effective methods on large scale, still, remains challenging. It is evident that high-end device fabrication and sophisticated device characteristics can be achieved with high-quality building blocks.^[11] From the perspective of “top-down” methods, electron beam lithography (EBL) provides excellent fidelity but

Dr. V. Gupta, S. Sarkar, O. Aftenieva, T. Tsuda, L. Kumar, D. Schletz, Dr. A. Kiriya, Prof. A. Fery, Dr. T. A. F. König
Leibniz-Institut für Polymerforschung Dresden e.V. (IPF)
Institute for Physical
Chemistry and Polymer Physics
Hohe Str. 6, 01069 Dresden, Germany
E-mail: koenig@ipfdd.de

Dr. V. Gupta, Prof. N. Vogel
Institute of Particle Technology
Friedrich-Alexander University Erlangen-Nürnberg
Cauerstrasse 4, 91058 Erlangen, Germany

 The ORCID identification number(s) for the author(s) of this article can be found under <https://doi.org/10.1002/adfm.202105054>.

© 2021 The Authors. Advanced Functional Materials published by Wiley-VCH GmbH. This is an open access article under the terms of the Creative Commons Attribution License, which permits use, distribution and reproduction in any medium, provided the original work is properly cited.

S. Sarkar
Department of Physics
Indian Institute of Technology Delhi
New Delhi 110016, India

J. Schultz
Leibniz-Institut für Festkörper- und Werkstofforschung
Institute for Solid State Research
Helmholtzstraße 20, 01069 Dresden, Germany

Prof. A. Fery
Physical Chemistry of Polymeric Materials
Technische Universität Dresden
Bergstraße 66, 01069 Dresden, Germany

Dr. T. A. F. König
Center for Advancing Electronics Dresden (cfaed)
Technische Universität Dresden
01062 Dresden, Germany

DOI: 10.1002/adfm.202105054

the subsequent etching steps, along with the accumulation of metal through physical vapor deposition, cause polydispersity and nonuniformity due to the arbitrarily oriented nanoscale grains.^[12,13] Other techniques such as scanning probe lithography,^[14] microcontact printing,^[15] dip-pen lithography^[16] either lack in terms of resolution or scalability. Recent reports revealed that post-fabrication thermal annealing of plasmonic NPs has the potential to reduce electron scattering and produce ultranarrow plasmonic resonances.^[17] In contrast, colloids formed via wet chemical synthesis under “bottom-up” methods are superior in terms of monodispersity, crystallinity, and surface functionalities.^[18–21] Hence, this results in lowering the damping of plasmon energy from defects, elastic and inelastic collisions, and phonons. However, to this end, the challenge remains to assemble these colloids with nanometer precision on a large scale in a controlled manner.

A combination of “top-down” and “bottom-up” methods such as capillary assisted particle-assembly (CAPA),^[22–24] DNA mediated assembly,^[25,26] electrophoretic deposition,^[27] electrostatic assembly,^[28] colloidal lithography^[29–31] have a wide prospect.^[32] However, there are still a variety of limitations in terms of cost-effectiveness, complete access to the colloid surface due to their residing into the template trenches, constrained scalability, and limited selection of colloid and target substrate for printing. To mitigate some of the issues, a recent method of template dissolution interfacial patterning (TDIP) has been introduced.^[33] Yet, this method is affected by various process parameters such as longer assembly duration, contact angle, humidity, temperature, dew point, and other environmental factors. On the other hand, nanoimprint lithography (NIL) has already shown its potential to overcome most of the contemporary challenges such as commercialization of the technique, on-chip patterning, lower consumption of stamp material with multiple usages of stamps.^[34] This simple yet powerful embossing concept utilizes a pre-structured elastomeric stamp in the desired dimension for pattern transfer on a target substrate.^[35] Predominantly, the use of micro and nano-imprint lithography has shown big potential in a multitude of applications, ranging from surface-enhanced Raman spectroscopy substrates such as plasmonic superlattices,^[36] designing bio-nano interfaces,^[37] hierarchically organized plasmonic mesostructures,^[38] plasmonic back reflector solar cells,^[39] nanobatteries,^[40] and nanoelectronics.^[41] A very recent article on NIL by Harshal et al. has acknowledged the superiority of the method over diverse fronts, however, lacking the application aspects.^[42] Thus it becomes important to demonstrate different possibilities with such an adaptable technique, especially in the domain of plasmonically enhanced photoconductivity and photocatalysis.

In this article, we show a quick, versatile, and maskless two-beam interference lithography technique in combination with soft molding with polydimethylsiloxane (PDMS) to produce efficient optoelectronic devices. Colloids of high optical quality arising from their homogeneous sizes, shapes, and defined crystallinity obtained from seeded growth wet-chemical synthesis technique can be easily arranged on various target substrates. We have printed 1D pure colloidal grating on transmission electron microscope (TEM) grid, glass, and silicon wafer substrate, gold film, dopable polymer semiconductor (DPS) film as well as titanium dioxide (TiO₂) slab waveguide on a centimeter scale. Overall, different periodicities of 1D gratings metallic photonic

crystals have been realized on conductive, dielectric, organic-inorganic semiconductor materials to showcase the versatility of the method. In our previous study, we used a prefabricated dielectric grating to assemble 1D colloid grating via CAPA toward achieving hybrid modes.^[43–45] In contrast, here, to the best of our knowledge, we report waveguide-plasmon polaritons (WPP) excited for the first time by a purely colloidal 1D lattice printed on TiO₂ slab waveguide via NIL on a centimeter scale. High-quality optical modes are achieved with a narrow line-width of 10 nm as compared to their EBL fabricated counterpart.^[46–48] To broaden the applicability, the modes supporting WPP are excited to qualitatively understand the charge transfer capabilities of the well-known Au/TiO₂ heterojunction toward hot carrier injection.^[49–51] Further, the enhanced light absorption due to WPP is utilized to harness light energy into chemical potential energy. Huang et al. recently proved that hybridized WPP modes can enhance hot electron generation, finally resulting in greatly accelerated reduction conversion at a low illumination intensity.^[52] Contrary to previous studies,^[44,51] we have excited the Au/TiO₂ interface with an off-normal excitation of 15° angle of incidence (AOI) since the plasmonic catalysis has a strong polarization dependency^[49] showing enhanced photocatalytic activity when the polarization direction is perpendicular to the Au/TiO₂ interface.^[49] Accordingly, we have used the MO dye oxidation as a probe reaction to study the hybrid WPP-induced catalysis. Thus, the technique can be employed in various fundamental studies of charge transfer, nanochemistry, and solid-state device fabrication. Study of plasmonic waveguide band formation on a TEM grid,^[35] out-of-plane lattice resonance (OPLR) from colloidal building blocks on a glass substrate, the coupling of OPLR with NP on mirror configuration on a gold film substrate, etc. are just to name such aspects.^[53,54]

2. Result and Discussions

The course of action to ensure a large-scale nanosphere imprint soft interference lithography is illustrated in **Figure 1**. The process begins with the fabrication of a master template (1D grating on a glass substrate (Figure 1a)) via laser interference lithography (LIL).^[24] Being a low-cost and energy-efficient procedure, this can be recommended as a suitable candidate for large-scale integration, as compared to the e-beam techniques. This high-resolution maskless pattern-printing technique has the capability to produce numerous kinds of patterns with varying duty-cycle, periodicity, depth, and pitch within a short span of time 2 to 3 min (for more details please refer to Figure S1, Supporting Information). Next, the replica of the master template is created by casting an elastomer, known as PDMS, onto the master. Generally, PDMS is preferred as the material of choice in NIL^[42] due to its elastic, yet inert nature and low surface energy. Flexibility being one of the key factors, allows PDMS a firm, thorough, and complete contact with the target substrate and leads to a high-quality assembly. After curing and peeling off, the polymer with an inverse structure is obtained which is referred to as ‘PDMS stamps’ in further discussions (Figure 1b). The height profile of the PDMS stamp and macroscopic intense diffraction color underlining the order of 1D grating over large areas are shown in Figure S2, Supporting Information. In the

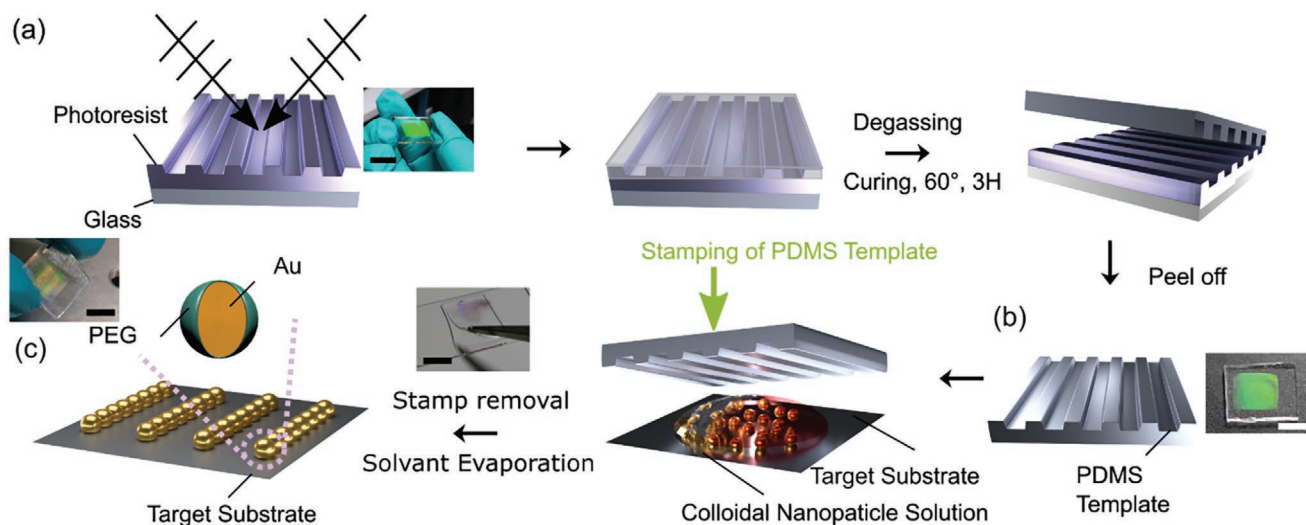


Figure 1. Schematic of the gold nanosphere imprint soft interference lithography process. a) Preparation of the solid master template by LIL, b) PDMS molding toward flexible inverse template formation, and c) arrangement of particles in 1D-lines on substrates using the flexible PDMS mold. Scale bars in photographs correspond to 1 cm.

actual printing process, the target substrate onto which the pattern has to be printed is first treated with oxygen plasma for surface activation, ensuring a uniform wetting behavior over the entire substrate. After the plasma treatment, an optimized concentration of 5 mg mL^{-1} and a volume of $5 \mu\text{L}$ colloidal ink is dispensed on top of the substrate, followed by the precise placement of the PDMS stamp. This colloidal ink consisting of defined crystallinity, monodisperse, atomically smooth gold nanospheres (as can be seen in Figure S3, Supporting Information) dispersed in water is allowed to dry completely at room temperature. Finally, the PDMS stamp is removed, leaving behind the pattern printed on the target substrate. Excess gold nanospheres, stuck in or onto the stamp, can be brought back to the solvent by ultrasonication, leading to further re-usage of the stamp. There are some important factors to be considered during the process, such as retaining the uniform thickness of the PDMS stamp. This is the key to produce an even pressure from its own weight, thus, ensuring the high-quality patterning over the large area. Since we are not applying external force (pressure) onto the stamp, the weight of each stamp is kept constant to 2.74 gm. The non-patterned region of the PDMS stamp is cut out before stamping to avoid wastage due to the formation of the particles on the target substrate outside the patterned area. The technique does not require adhesion layers for printing and rather relies on adhesive forces between PDMS and target surfaces.^[36] Due to the soft nature of PDMS, it can conform into contact with the substrate; however, due to low adhesion forces, it can be removed again after the printing without damaging the precise alignment. Hence, this facilitates the direct contact between the colloids and the targeted substrate and also imparts precision in the printing process. Further, the technique forbids the system to be influenced by the refractive index of the adhesive layer and provides full access to the colloid surface in contrast to the previous CAPA.^[33] The sphere is a choice of shape because of its minimal surface contact with the substrate. Once adapted for spherical morphology, other isotropic geometries (i.e., nanocubes) thus become more

feasible because of their enhanced surface contact area with the target substrate. The technique is less prone to environmental factors, highly reproducible, does not require an extra adhesive or sacrificial layer, can be directly employed on surfaces with varying topography and hydrophobicity, and also not limited by the material choice, shape, or size of the colloid and the target substrate. Above all, it provides complete access to the gold NP surface through the production of free-standing layers.

We apply the technique to transfer the gold NP grating onto a range of different target substrates, which vary in terms of topography, conductivity, and wettability. **Figure 2a** shows the successful assembly on different target substrates ranging from small dimensions (3.05 mm) of a TEM grid to '1.5 cm by 1.5 cm' (patterned areas) on glass substrates, gold mirrors, and semi-conducting polymer thin films. The method has the potential to transfer the patterns on large scale as well by using wrinkles as a stamp.^[55] By combining the LIL with NIL, various types of patterns can be achieved. **Figure 2b** shows microscopy images for each target substrate with two different illumination configurations. In the first configuration (top images), the incident electric field (e-field) is parallel to the particle lines, whereas, in the second configuration (bottom images), the e-field is considered perpendicular to the same particle lines. The different observed colors reflect the different absorption and scattering of the particles depending on whether they are excited along the lines or perpendicular to them.^[56] Well-defined placement of the colloids and large-scale assembly on a TEM grid and glass substrate can be seen in Figures S4 and S5, Supporting Information. **Figure 2c** shows scanning electron microscope (SEM) and TEM images of the fabricated nanopatterns on various target substrates. Drying of the ligand shell inherently leads to slight shrinkage of the particles, which causes the printed lines to break up into oligomeric chains. We use image analysis to investigate the yield (as can be seen in Figure S6, Supporting Information), which shows that 75% of the lines are covered with particles with an average particle chain length of around 8 particles. The assembly process is dependent on substrate

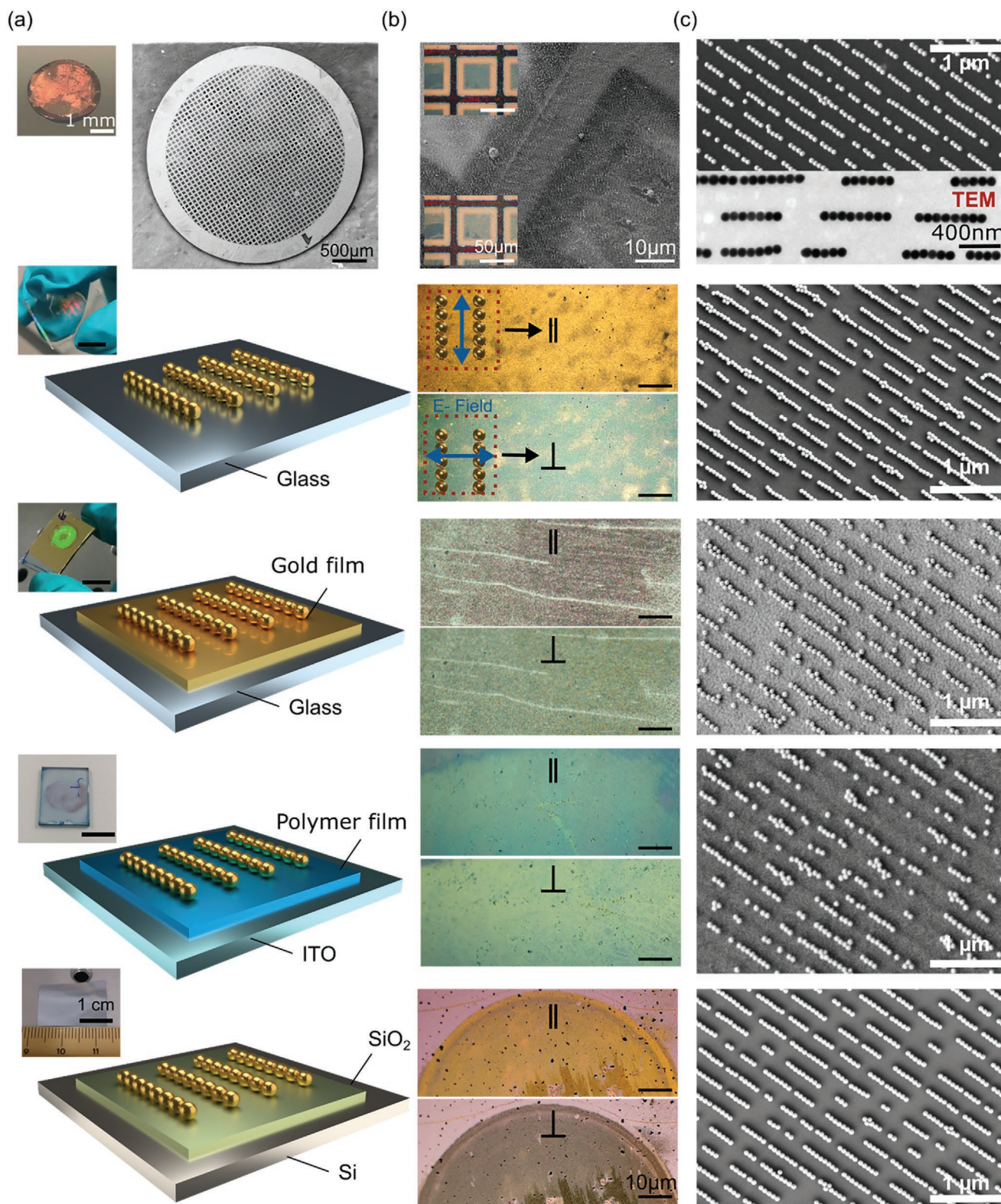


Figure 2. a) Schematic of the 1D gold nanosphere imprint soft interference lithography on various substrates. Inset shows photographs of actual fabricated samples. b) Optical micrographs of the assemblies with polarized light illumination parallel (denoted as ||) and perpendicular (denoted as ⊥) to particle chains respectively. The blue arrow denotes the electric field (e-field) direction. c) SEM and TEM images of the particle lines on the corresponding target substrate. The Scale bars in SEM images are 1 μm.

roughness. The assembly yield on commercial substrates such as silicon wafer, TEM grid, and microscope glass slide is better (in the range of 70%) as compared to the electron-beam deposited materials such as TiO_2 and gold film. The polymer film was coated with spin coating method and hence possesses more surface roughness as compared to the commercial substrate. In order to reveal the 2D aspect of the technique, a 2D square pattern is printed on glass using a nanopillar template as a stamp as shown in Figure S7, Supporting Information. To extend further application-oriented features of the assembly method, colloids are printed on naphthalenediimide (NDI)-based pi-conjugated polycations. Structure of an NDI-based pi-conjugated polycations used in this work as an n-doped

semiconducting polymeric interlayer is shown in Figure S8, Supporting Information. These solution-casted NDI polymer films can be doped with electrons, thus falling into the category of DPS. In this regard, the combination of the optical structures (1D colloidal grating) and the NDI polyelectrolytes are promising for an air-stable hot electron extraction system.

Having established the interference lithography-based NIL method, we demonstrate functional optical properties arising from such colloidal grating assemblies. We focus on hybrid WPP structures, which we produce by printing colloidal plasmonic gratings onto a TiO_2 semiconductor thin film. Figure 3a shows a schematic illustration of the targeted structure with assembled NP chains over a thin film of semiconducting TiO_2 layer, coated

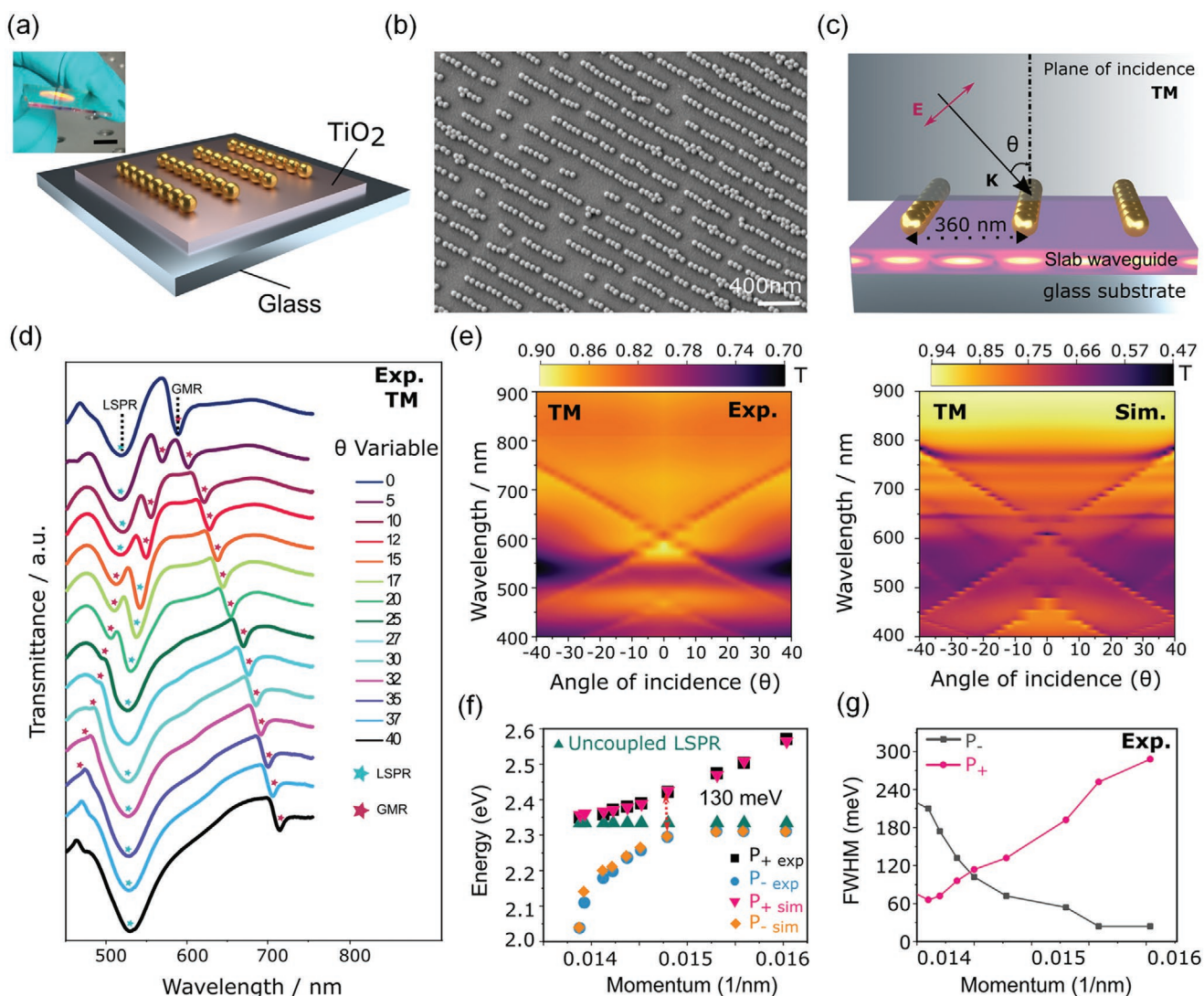


Figure 3. Optical properties of hybrid WPP structures prepared by NIL assembly of colloidal chains on a semiconductor thin film. a) Schematic of the 1D gold nanosphere imprint soft interference lithography on TiO_2 waveguide, deposited on a glass substrate. b) SEM image of the particle lines printed onto the TiO_2 surface. c) The optical scheme to establish hybrid-waveguide plasmon polariton formation using the principles of guided-mode resonance. Plasmonic grating crafted out of the gold nanoparticle lines diffracts the incoming plane-wave where polarization-specific waveguide modes can be confined to the semiconductor waveguide. Electric field orientation conveys excitation of the transverse magnetic (TM) modes. d) Optical transmittance spectra of the fabricated hybrid structure under TM polarized incidence. Avoided-crossing is observed between the plasmonic LSPR and the photonic GMR_1 mode upon variation of the angle of incidence (AOI). e) Experimental vs. simulated (FDTD) optical band diagram for TM polarized incidence. f) Energy dispersion curves with dots corresponding to the Eigen-energies of the polariton states (P^- and P^+) calculated from experimental as well as simulated transmittances. g) Spectral line widths for the upper and lower (P^+ and P^-) energy branches calculated from experimental data.

on a glass substrate. Such hybrid chains on a semiconductor waveguide have been recently explored by Sarkar et al.,^[43,44] where the particle chains were arranged within additional photoresist grating channels, patterned on the TiO₂ layer through interference lithography.^[43] While the structure could be achieved in a straightforward assembly technique, it had a major drawback of the presence of additional photoresist layers as a barrier to the charge transfer processes.^[55] In the present case, we have successfully eliminated the chances of hindrances being caused by any residual photoresist layer by directly transferring the NP chains. Importantly, to ensure that the plasmonic particles directly interface with the semiconductor, samples were treated with oxygen plasma to remove the ligand shell around the particle. Thus, the plasmonic chains become an active component of the hybrid system, taking part in diffraction and guided mode-resonance effects. Interestingly, the guided-mode resonance (GMR) condition is satisfied for the first time using a purely colloidal grating from the template onto the TiO₂ waveguide.

Figure 3b provides an SEM image of such successful transfer of the NP chains on the TiO₂ surface. We investigate the optical properties of the hybrid resonating structure both by experiment and simulation. Figure 3c shows the geometry used for finite difference time domain (FDTD) based simulations. A transverse-magnetic (TM) polarized plane wave is diffracted by the NP chain grating, resulting in the formation of guided modes within the high-indexed semiconductor layer. Figure S9a-iii, Supporting Information further provides direct proof of meeting the GMR condition through the electric field distribution ($|\vec{E}| = \sqrt{E_x^2 + E_y^2}$) similar to conventional GMR cases under TM polarization. Note, that unlike the previous demonstration of hybridization^[43,44] using longitudinal plasmonic chain modes,^[56] the novelty of the present work lies in introducing transverse plasmonic chain modes into the hybridization picture. Figures S9 and S10, Supporting Information show these two dominant resonances of localized surface plasmon resonance (LSPR) and GMR under different cross-sections of the 3D electromagnetic simulation. The choice of the periodicity of 360 nm with a 200 nm waveguide thickness allows excitation of uncoupled plasmonic and photonic resonances under normal TM incidence. The dispersive nature of GMR is utilized to interact with LSPR, resulting in spectral doublets with anti-crossing behavior: a coherent superposition of the plasmonic and the TM₀ waveguide modes. However, as the AOI is increased, as shown in transmittance plots in Figure 3d, the photonic GMR mode becomes non-degenerate, resulting in splitting into GMR₁ and GMR₊₁ modes.^[57] Anticrossing behavior between the resonant plasmonic and photonic channels reveals the hybridization signatures as an interplay between the LSPR and GMR₁ mode at around 15-degree incidence. Figure 3e shows an agreement of the optical band diagrams corresponding to the experimental as well as simulated TM transmittances, arranged in intensity contour plots. The energies of excited hybrid states, P+ and P- are measured from the dip positions of the transmittances (both experimental and simulated) and plotted as a function of momenta (related to incidence angle) in Figure 3f. However, a Rabi splitting of 130 meV is observed. The spectral characteristics of these hybrid states are further evaluated in Figure 3g in terms of the resonant line-widths. The measured extinction curve is shown in Figure S11, Supporting Information where a narrow FWHM of 10 nm is determined via curve fitting for the hybrid case with an AOI of 15°.

A two terminal^[58,59] hybrid GMR device supporting WPP modes under a hot-electron detection scheme is shown in **Figure 4a**. Two gold electrodes with a thickness of 60 nm are deposited on top of the devices through a shadow mask to yield a 220 μm wide strip. The photoconductivity was measured in between the source and drain under a bias voltage of 1 V.

More information regarding the two-terminal device is provided in Figure S12, Supporting Information. Note that the 1D lines continue for a few micrometers on both electrodes to ensure that the current is already injected into the strongly coupled system before reaching the active channel.^[60] The active channel is the distance between the source and drain, which in the present case is 350 μm. It is known that plasmons predominantly exhibit radiatively damped oscillations (re-emission of a photon).^[61] Thus, by use of WPP-supported hybrid-GMR structure, the strong suppression in radiative losses (exhibited via narrow line-width) promotes nonradiative relaxation (Landau damping), a process that is argued to generate hot-electrons.^[61] Hence, the mode at 545 nm with the sharpest spectral line width of 10 nm under AOI 15° is selected. In theory, direct contact between metal and semiconductor form a Schottky junction, as shown in Figure 4b. Nonradiative decay of plasmons inside the metal constituent of the hybrid GMR device can take place in the time frame of 1–100 fs,^[47] followed by the excitation of the WPP modes. This results in electron-hole pairs (hot-carriers) formation in the metal. With subsequent electron-electron collision processes, the generated hot carriers can cross the Schottky barrier, provided that their energy exceeds the Schottky barrier height and the momentum lies inside the escape cone.^[62] Taking all this into account, the sample is illuminated with several LEDs. The intensity and bandwidth data for LEDs are shown in Figure S13, Supporting Information. Since the 565 nm LED has the best overlap with the extinction spectra which is relatively near at 15° AOI, maximum photocurrent was detected as shown in Figure 4c. The setup to measure the photocurrent is shown in Figure S14, Supporting Information. In the case of the TiO₂ layer, oxygen vacancies can produce a defect/trap state just below the conduction band of the TiO₂.^[51] Electrons from the top of the valance band can jump into these states and with possibilities of contribution in the photocurrent generation.^[51] Aiming to rule out this possible effect, we deposited the electrodes on bare TiO₂ film and illuminated it with the same LEDs. The resulting photocurrent and responsivity results (see Figures S15 and S16, Supporting Information) demonstrate that the TiO₂ is almost free of defect-states or interfacial oxide layers. The crystallinity of the deposited TiO₂ thin film is crosschecked to be in anatase phase, as provided in Figure S17, Supporting Information. It is necessary to consider that the so-called “photocurrent” is different from that in photovoltaic devices where all electrons in the collected current are fully induced by the absorbed photons. Here the current is generated by the voltage bias (1 V) at the two sides of the TiO₂ slab and its magnitude is modulated by light absorption due to change in the conductivity of the TiO₂ slab. The important mechanism to cause the “photocurrent” modulation is the injection of the plasmon-induced hot electrons over the Schottky barrier from Au into the TiO₂ conduction band to become free electrons. A similar device could also be used for light addressable potentiometric sensors and photodetectors. To compare the presently observed hybrid device photoresponse,

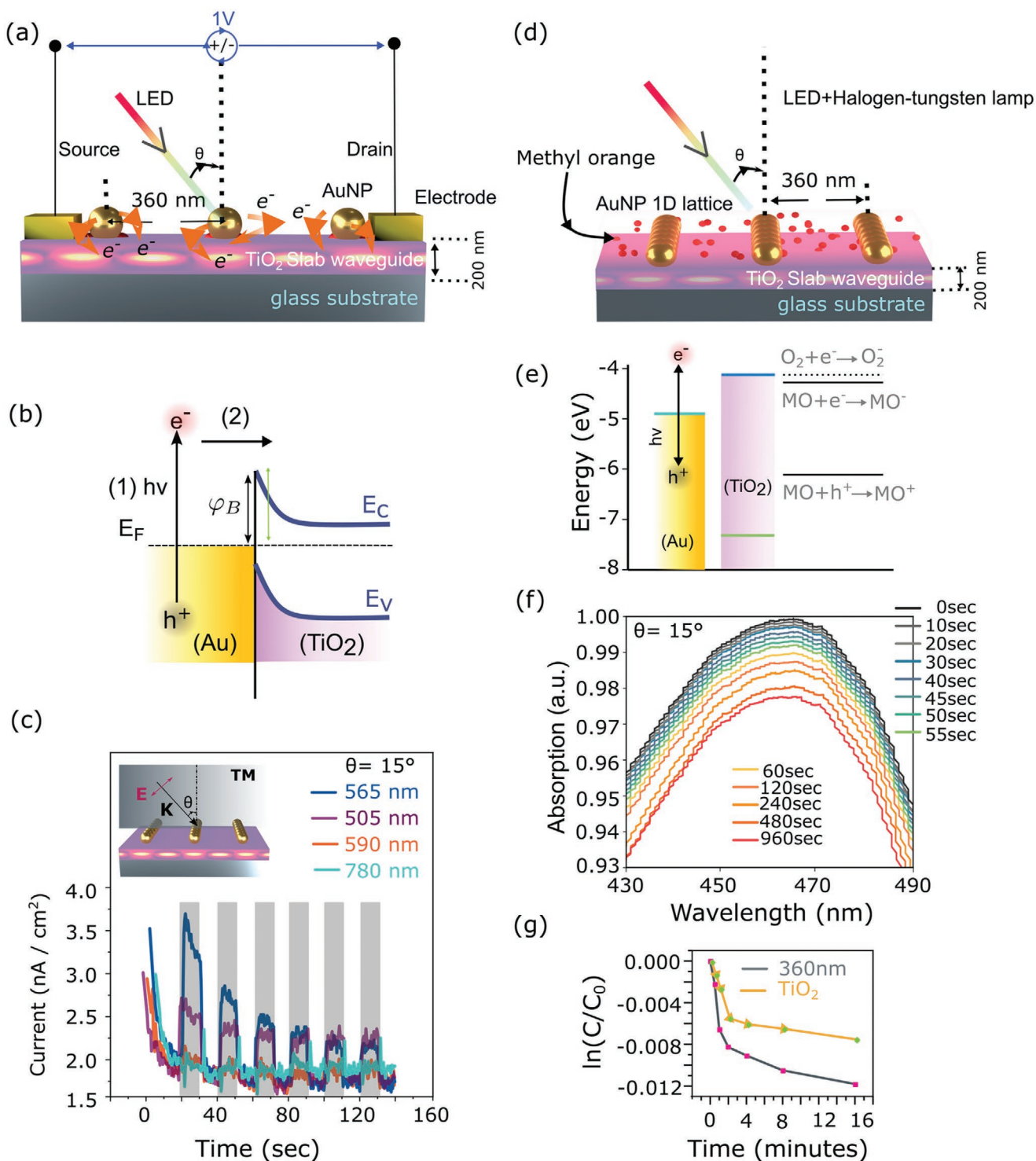


Figure 4. Plasmon-induced charge transfer and photocatalysis mechanism in nanodevice: a) A GMR device is depicted which constitutes a 200 nm thin film of TiO_2 deposited and a pure colloidal grating with a periodicity of 360 nm. Various wavelengths are incident on the device with an AOI close to 15° . Generated hot electrons are shown as the symbol e^- and measured with the bias voltage of 1 V through gold electrodes. b) The charge transfer mechanism and band diagram of an Au/ TiO_2 Schottky junction is shown. c) Photoresponse recorded with different LEDs launching light at an AOI $\approx 15^\circ$. Gray stripes show the duration for which the light source was on whereas the white area depicts the off duration for the different wavelengths. d) A drop of MO dye solution is placed on top of the GMR device to investigate the photocatalytic properties. e) Energy band diagram and reaction mechanism of decomposition of the MO dye. f) Time-evolved absorbance spectrum of dye in solution. g) Change in MO concentration as a function of time (shown in logarithmic scale).

Table 1. Comparison of current (/density) data under a similar range of bias voltages.

Year	Material	Fabrication	Mechanism	Wave-length	Current (/density)	Bias voltage	Ref.
2015	PDI2EH-CN ₂ organic semiconductor	Spin coated thin films on FIB milled hexagonal array of Ag	Strongly coupled plasmon modes	745 nm	50 nA	1 V	[59]
2016	Core-shell Au-TiO ₂	Wet chemical synthesis	LSPR excited electrons	400–800 nm (1 sun illumination)	200 nA	0.2 V	[60]
2018	3D tandem plasmonic Au/TiO ₂ nanodiodes	Sol-gel coated and e-beam deposited thin films	LSPR excited hot electrons	563 nm (9 mW cm ⁻²)	150 nA	1 V	[63]
2019	MaPbI ₃ -modified plasmonic Au/TiO ₂ nanodiodes	Spin coated thin film	LSPR excited hot electrons	563 nm (9 mW cm ⁻²)	500 nA	1 V	[64]
2020	p-type organic semiconductor (rr-P3HT)	Spin coated thin films on FIB milled hexagonal array of Ag	Strong coupling between surface plasmon and organic semi-conductor	610 nm	10 nA	1 V	[58]
2020	ITO-TiO ₂ -Au	TDIP and soft lithography using e-beam made master	LSPR generated hot-electrons	>450 nm	20 nA cm ⁻²	–	[65]
2021	Glass-TiO ₂ -AuNP chains	Nano imprint lithography	Waveguide-plasmon polariton under strong coupling	565 nm	4.0 nA cm ⁻²	1 V	Current work

Table 1 displays some recently reported architectures operating under various plasmonic excitation schemes. Apart from NP chain based plasmonic excitation, Sarkar et al. also discussed the hot electron generation due to LSPR excitation on randomly distributed particles over TiO₂ thin film (200 nm)/glass substrate.^[44] In such randomly distributed non-hybrid particle system, similarly measured photocurrent was found to be in the range of 0.5 nA cm⁻². In contrast, the photocurrent for GMR hybrid mode at a lower wavelength of 565 nm is seven-fold enhanced and lies in the range of 3.5 nA cm⁻² as shown in Figure 4c. The plasmonic-photonic coupling via the generation of WPP highlights the benefits of admixing colloidal chemistry with NIL, thus making up to this list.

Further, we demonstrate the enhanced photocatalytic activity of the hybrid device by studying the decomposition of the organic dye MO. A solution of MO dye is placed on top of the hybrid GMR device, as shown in Figure 4d. The sample was illuminated by the broadband halogen lamp (0.25 mW, normal incidence) together with the LED source (2.7 mW, oblique illumination at ≈15°) at 565 nm. MO being an azo dye, is considered to be stable and difficult to be oxidized at room temperature, in dark.^[63] For illumination with energies higher than the band-gap energy (ultraviolet (UV) illumination) of TiO₂, the reduction of the dye is a well-known process via direct hole transfer from TiO₂.^[63] Here, we show the decomposition of the dye with the visible light photon energies, which is well below the band-gap of TiO₂. The work-function of Au, conduction and valance band of bulk TiO₂,^[65] the redox potential of MO in solution,^[66] and the reaction mechanisms are shown in Figure 4e. To measure the oxidation rate of the dye, we avoided exposure to the ambient light, while the sample was illuminated by the broadband halogen lamp together with the LED sources at fixed angles. The rate of oxidation was estimated from the time-resolved absorption spectra. Without the LED, the change in absorption intensity (0.1%) within a similar period was considered negligible (as shown in Figure S18b, Supporting Information) due to ≈ten times lower power of the broadband light source. The reference absorption spectrum of

dye with only a TiO₂ layer is also shown in Figure S18a, Supporting Information under similar conditions (broadband illumination combined with the LED at 565 nm). The possibilities of direct photo-decomposition of dye in very unlikely, since the dye shows an extremely low absorption of 565 nm wavelength.^[67] This also eliminates the chance of a possible decomposition pathway where photoexcited MO transfers the charge to Au or TiO₂.^[68] We, therefore, propose the following mechanism for photodegradation. At first the photons with energies exceeding the height of the Schottky barrier can excite the WPP. During the decay process, these collective excitations may possibly transport a charged electron (e⁻) into the semiconductor, leaving behind a ‘hot-hole’ in the metal. Being a photochemical process, the photo-generated electrons and holes react with H₂O and O₂ in the MO aqueous solution to produce highly active oxidizing species, which in turn results in the photodecomposition of MO. Hence both hot holes and hot electrons take part in the catalysis process.

Thus, the decrease in the concentration of MO is monitored through the absorption spectrum. The whole spectra of the GMR device + MO are shown in Figure 4f for this wavelength range of interest (430 to 490 nm). During this measurement, both LED (2.7 mW) and tungsten-halogen light sources (0.25 mW) were illuminated; however, due to the ten times lower power of tungsten halogen source, the decomposition of MO can only be only considered for LEDs. Figure 4g has been obtained by simply taking the logarithmic of the absorption values shown in Figure 4f for clear distinguishability of the dye decomposition rate for both the cases of the GMR device and the bare TiO₂. Hence, it is evident that the WPP supported structures can tackle the essentials of photocatalysis in terms of enhancing the visible light absorption via device engineering, improving the charge separation lifetime by adjusting the Schottky barrier height via prudent material selection,^[69] and providing very large energy densities at the near field with strong light confinement. Apart from this, the WPP excitation under TM polarization also provides a component of the electric field vector perpendicular to the Au/TiO₂ interface which, being the exact active catalysis site, leads to the more enhanced catalytic activity.^[49]

3. Conclusion

In summary, we present an inexpensive, fast, facile, and reproducible technique that has the potential to print the desired structure with high resolution over large areas, using colloidal ink as imprint resist. The technique, as a combination of IL and NIL, is applied to fabricate 1D metallic photonic crystals on various target substrates with varied topography, conductivity, and hydrophobicity. Fundamentally, the method is non-destructive, flexible in terms of the target substrate, provides full access to the colloid/substrate interface and the colloid itself. It also facilitates multiple uses of the PDMS stamp, clean printing of patterns, and broadening of the scope in terms of size, shape, and choice of material. Above all, it possesses the capability for roll-to-roll integration and commercialization. In this article, we have shown a high-quality factor (Q-factor) WPP modes, achieved via arranging pure colloidal grating into appropriate design geometry. A narrow line-width, down to 10 nm, is achieved which is superior to their top-down counterparts.^[46] Despite high-quality optical modes, the high photocurrent efficiency remains a challenge in the case of colloids where an inescapable ligand shell is required to make them stable in the colloidal suspension. In a recent article, similar issues have been raised in a different way.^[33] There can be several strategies to tackle this issue; one such solution may be to directly synthesize photoconductive polymer coatings around the plasmonic building block.^[70] Further, in heterogeneous colloidal engineering,^[71] conductive ligands can also be used as an anchor group to attach organic ligands.^[72] With a view toward the applicability of the method, we have shown a clear correlation between excitation of WPP in pure gold nanosphere grating supported on TiO₂ waveguide, and the decomposition of MO dye as a consequence of hot-electron transfer from 1D colloidal Au grating into TiO₂ under visible light illumination. We envisage that the method is a stepping stone for the printing of various colloidal geometries and holds potential in applications in colloidal nanobiophotonics, nanochemistry, and nanosensing.

4. Experimental Section

Template Fabrication: To produce a structured polymer stamp, a soft lithography technique was employed. First, the master template was fabricated by the means of LIL on a glass substrate. For this, microscopy glass slides were divided into individual pieces (2 × 2 cm) and cleaned with isopropyl alcohol and ultrapure water in a 1:1 ratio by sonication for 20 min at 80 kHz. Positive photoresist (mr-P 1202LIL, micro resist technology GmbH, Germany), diluted with a thinner solution (ma-T 1050, micro resist technology GmbH, Germany) to a 1:1 ratio, was spin-coated onto the substrate. Optimized spin parameters of 3000 rpm, acceleration of 1000 rpm s⁻¹, and total spin time of 33 s produced a thin film of 80 nm thickness, as confirmed by spectroscopic ellipsometry (RC2-DI, J.A. Woollam Co., Inc.). The coated substrates were baked at 95 °C for 60 s and further exposed to the 325 nm laser with a dose of 12 mJ cm⁻². The backside of the substrate was covered with black adhesive tape to avoid unnecessary reflections. To develop the exposed photoresist, the sample was submerged into the developer (mr-D 374/S, micro resist technology GmbH, Germany) for 40 s, rinsed with ultrapure water, and dried under a stream of nitrogen. The total patterned area was in the shape of a circle with a diameter of 1.5 cm. The resulting periodic structure was modified via gas-phase deposition with

trichloro(1H,1H,2H,2H-perfluorooctyl)silane (448931, Sigma Aldrich) at 60 °C for 3 h, and then molded with SYLGARD 184 Silicone Elastomer (The Dow Chemical Company, USA) in a 10:1 mixing ratio with the curing agent and cured for 3 h at 60 °C. After that, the PDMS stamp was peeled off from the master template and examined by the atomic force microscopy technique, revealing a 1D grating with a periodicity of 360 and 80 nm depth (the details can be found in Figure S2, Supporting Information).

Nanosphere Synthesis: The synthesis of spherical gold NPs was carried out through a seed-mediated growth process.^[55] As a result, gold NPs with a diameter of 76.9 ± 1.5 nm (averaged over 100 particles) covered with hexadecyltrimethylammonium chloride were obtained. In summary, the NPs stabilized with polyethylene glycol (PEG) in water were synthesized in three main steps. First, Wulff seeds were produced by reducing tetrachloroauric acid (HAuCl₄) with sodium borohydride (NaBH₄) in the presence of hexadecyltrimethylammonium bromide (CtaB). This process results in large 2 nm monocrystalline NPs. Next, these particles were enlarged with the aid of two further successive synthesis steps until they reached the desired particle diameter. During the growth process, HAuCl₄, ascorbic acid, and CtaC serve as Au precursors, reducing agents, and stabilizing agents, respectively. To achieve kinetic control over the reaction and thus to modulate the particle shape, a syringe pump system was used for the last growth step. In the last step, the particles were washed and cleaned by a centrifugation process and fixed to a surfactant concentration of 2 mM. In order to give the NPs in the colloidal suspension of water long-term colloidal stability, a ligand exchange from CtaC to PEG-6k-SH^[36] was carried out.

NDI Polymer Synthesis and Thin Film Preparation: NDI polymer was synthesized according to the literature.^[73] The film was formed on an unpatterned ITO substrate (S111, Ossila), the substrate was washed with acetone and isopropanol in an ultrasonic bath beforehand. After the UV treatment of the substrates, the polymer film was formed from a trifluoroethanol solution (10 gm L⁻¹) by spin coating. The formed film thickness was 100 nm.

Thin Film Deposition: The e-beam deposition was achieved using a Hex-L modular thin film deposition system (Korvus Technology) teamed with a Telemark e-beam source. Stage rotation was applied during the deposition. The Telemark e-beam source was equipped with four rotatable pocket sources. A 5 nm Ti layer was deposited, followed by a 50 nm Au layer. The films were deposited at a constant deposition rate of 1 Å s⁻¹ and a chamber pressure of 1.5 × 10⁻⁶ mbar. The thin film thickness was monitored using a calibrated quartz crystal thickness monitor (QCM); for better accuracy, the tooling factor was optimized for each layered material. Similarly, a 200 nm TiO₂ film was deposited on a glass substrate at a constant deposition rate of 1 Å s⁻¹ and a chamber pressure of 1.5 × 10⁻⁶ mbar.

Catalysis Measurement via Bright Field Spectra and LED Excitation: For the spectroscopic measurement of the catalytic activity, a Nikon Ti-U inverted microscope in transmission mode was used. The sample was illuminated by a tungsten-halogen light source through a bright-field condenser (LWD, NA 0.52, Nikon, Japan), avoiding the ambient light. The data were collected through a 60× air objective (CFI S Plan Fluor ELWD, NA 0.7, Nikon, Japan) by an IsoPlane-160 spectrometer and a PIXIS 256 charge-coupled device camera (Princeton Instruments). A water-dispersed solution of MO dye (1.53 × 10⁻⁴ mol L⁻¹, 500 μL) was drop-casted on the sample surface, covering the entire active area. To initiate catalytic activity, the sample was additionally illuminated by a 565 nm LED light source (2.7 mW power). The spectra were collected every 5 s until 30 s, then in 15 s steps until 1 min, and then after 2, 4, 8, and 16 min after the moment of switching on the LED light and the start of the reaction. The measured spectra were corrected by subtracting the dark current at the detector and normalizing against the reference spectra collected from a sample, where MO dye was replaced by water, at the corresponding time steps.

Optical Band Diagram: The UV-vis-NIR Spectrophotometer (Cary 5000, Agilent Technologies) was used to record the transmission spectra.^[74] Further, the sample was rotated in both positive and negative

directions with a mechanized stage and the detector was kept constant to record the dispersion relation. A polarizer was used to investigate the effect of both the polarization (pol), s-pol (transverse electric, TE), or p-pol (TM) where the electric fields were out of the plane and in-plane to the plane of incidence, respectively.

Photoresponse Measurement: Metal (Au) electrodes (Au, Layer thickness: 60 nm, channel length: 350 μm , width: 4500 μm) were deposited by e-beam evaporation applying a shadow mask. The electrodes were placed parallel to the 1D particle chains structure. The photoresponse was measured and recorded by a Keithley source meter (2612B, Keithley). LED lights from Thorlabs, with a wavelength of 365, 505, 565, 590, 660, 780 (M780L3), and 1050 nm (M1050L4) were used as light sources. All the LEDs were operated via a controlling unit (DC4100). Light was irradiated at an angle from the top of the device, and the distance between LEDs and devices was kept at 2 cm. The power of the LED sources was measured by a silicon photodetector connected to an optical power meter. For photocurrent detection, DC bias (1 V) was applied between electrodes. All the measurements were conducted under ambient conditions.

SEM/TEM: A NEON 40 FIB-SEM workstation (Carl Zeiss Microscopy GmbH, Oberkochen, Germany) was used in order to capture the scanning electron micrographs. The TEM data were acquired using an FEI Tecnai T20 microscope at 200 kV acceleration voltage.

FDTD Simulations: A commercial-grade simulator based on the FDTD method was used to perform all the calculations (FDTD: 3D Electromagnetic Simulator).^[75] For the simulation of the optical response, a plane wave source was used and the frequency points were set equal to that of the wavelength range. Monitor boxes (transmission monitors normally maintained on the substrate) were used to obtain the optical responses of the systems. For the dielectric function of gold, the Palik^[76] data were fitted using six coefficients with an RMS error of 0.2. For the TiO₂ layer and the glass substrate, optical constants were used from Sarkar et al.^[43] The mesh size in the FDTD region was set to auto non-uniform with an additional 2 nm mesh overlay applied to the arranged particle geometry. Periodic boundary conditions were applied for the X and Z directions with perfectly matched layers along the Y direction. All simulations reached an automatic stop of at least 10⁻⁷ before reaching a simulation time of 300 fs.

Supporting Information

Supporting Information is available from the Wiley Online Library or from the author.

Acknowledgements

V.G. and S.S. contributed equally to this work. This project was financially supported by the Volkswagen Foundation through a Freigeist Fellowship to T.A.F.K. V.G. and N.V. acknowledge the European Union's Horizon 2020 research and innovation program for funding under grant agreement No. 861950, project POSEIDON. O.A. and T.A.F.K. acknowledge the Deutsche Forschungsgemeinschaft (DFG) within the project 404818834 for financial support. N.V. acknowledges support from the Interdisciplinary Center for Functional Particle System (FPS) at FAU Erlangen-Nürnberg. J.S. received funding from the Deutsche Forschungsgemeinschaft (DFG, German Research Foundation) under Germany's Excellence Strategy through Würzburg-Dresden Cluster of Excellence on Complexity and Topology in Quantum Matter—ct.qmat (EXC 2147, project-id 390858490). The authors are thankful to Mr. Michael Göbel for performing the XRD analysis.

Open access funding enabled and organized by Projekt DEAL.

Conflict of Interest

The authors declare no conflict of interest.

Data Availability Statement

The data that support the findings of this study are available from the corresponding author upon reasonable request.

Keywords

colloidal nanospheres, nanoimprint lithography, photocatalysis, plasmon-induced charge transfer, waveguide-plasmon polariton

Received: June 7, 2021

Published online: June 29, 2021

- [1] N. J. Halas, S. Lal, W.-S. Chang, S. Link, P. Nordlander, *Chem. Rev.* **2011**, *111*, 3913.
- [2] J. H. Fendler, F. C. Meldrum, *Adv. Mater.* **1995**, *7*, 607.
- [3] Y. Zhang, S. He, W. Guo, Y. Hu, J. Huang, J. R. Mulcahy, W. D. Wei, *Chem. Rev.* **2018**, *118*, 2927.
- [4] R. Chikkaraddy, B. De Nijs, F. Benz, S. J. Barrow, O. A. Scherman, E. Rosta, A. Demetriadou, P. Fox, O. Hess, J. J. Baumberg, *Nature* **2016**, *535*, 127.
- [5] J. R. Mejía-Salazar, O. N. Oliveira, *Chem. Rev.* **2018**, *118*, 10617.
- [6] S. Li, P. Miao, Y. Zhang, J. Wu, B. Zhang, Y. Du, X. Han, J. Sun, P. Xu, *Adv. Mater.* **2020**, *33*, 2000086.
- [7] M. Zhang, M. Pu, F. Zhang, Y. Guo, Q. He, X. Ma, Y. Huang, X. Li, H. Yu, X. Luo, *Adv. Sci.* **2018**, *5*, 1870063.
- [8] J. Mun, M. Kim, Y. Yang, T. Badloe, J. Ni, Y. Chen, C.-W. Qiu, J. Rho, *Light: Sci. Appl.* **2020**, *9*, 139.
- [9] O. Aftenieva, M. Schnepf, B. Mehlhorn, T. A. F. König, *Adv. Opt. Mater.* **2020**, *9*, 2001280.
- [10] M. Kauranen, A. V. Zayats, *Nat. Photonics* **2012**, *6*, 737.
- [11] Y. Fang, M. Sun, *Light: Sci. Appl.* **2015**, *4*, e294.
- [12] P. Nagpal, N. C. Lindquist, S. H. Oh, D. J. Norris, *Science* **2009**, *325*, 594.
- [13] M. Hegner, P. Wagner, G. Semenza, *Surf. Sci.* **1993**, *291*, 39.
- [14] R. Garcia, A. W. Knoll, E. Riedo, *Nat. Nanotechnol.* **2014**, *9*, 577.
- [15] J. L. Wilbur, A. Kumar, E. Kim, G. M. Whitesides, *Adv. Mater.* **1994**, *6*, 600.
- [16] X. Liu, L. Fu, S. Hong, V. P. Dravid, C. A. Mirkin, *Adv. Mater.* **2002**, *14*, 231.
- [17] S. Deng, R. Li, J. E. Park, J. Guan, P. Choo, J. Hu, P. J. M. Smeets, T. W. Odom, *Proc. Natl. Acad. Sci. U. S. A.* **2020**, *117*, 23380.
- [18] N. R. Jana, L. Gearheart, C. J. Murphy, *Langmuir* **2001**, *17*, 6782.
- [19] Y. Zheng, X. Zhong, Z. Li, Y. Xia, *Part. Part. Syst. Charact.* **2014**, *31*, 266.
- [20] G. González-Rubio, P. Díaz-Núñez, A. Rivera, A. Prada, G. Tardajos, J. González-Izquierdo, L. Bañares, P. Llombart, L. G. Macdowell, M. Alcolea Palafox, L. M. Liz-Marzán, O. Peña-Rodríguez, A. Guerrero-Martínez, *Science* **2017**, *358*, 640 LP.
- [21] G. González-Rubio, T. M. de Oliveira, T. Altantzis, A. La Porta, A. Guerrero-Martínez, S. Bals, L. Scarabelli, L. M. Liz-Marzán, *Chem. Commun.* **2017**, *53*, 11360.
- [22] V. Flauraud, M. Mastrangeli, G. D. Bernasconi, J. Butet, D. T. L. Alexander, E. Shahrabi, O. J. F. Martin, J. Brugger, *Nat. Nanotechnol.* **2017**, *12*, 73.
- [23] T. Kraus, L. Malaquin, H. Schmid, W. Riess, N. D. Spencer, H. Wolf, *Nat. Nanotechnol.* **2007**, *2*, 570.
- [24] V. Gupta, P. T. Probst, F. R. Goßler, A. M. Steiner, J. Schubert, Y. Brasse, T. A. F. König, A. Fery, *ACS Appl. Mater. Interfaces* **2019**, *11*, 28189.
- [25] C. A. Mirkin, R. L. Letsinger, R. C. Mucic, J. J. Storhoff, *Nature* **1996**, *382*, 607.

- [26] J. Ye, R. Weichelt, U. Kemper, V. Gupta, T. A. F. König, A. Eychmüller, R. Seidel, *Small* **2020**, *16*, 2003662.
- [27] H. Zhang, Y. Liu, M. F. S. Shahidan, C. Kinnear, F. Maasoumi, J. Cadusch, E. M. Akinoglu, T. D. James, A. Widmer-Cooper, A. Roberts, P. Mulvaney, *Adv. Funct. Mater.* **2020**, *31*, 2006753.
- [28] D. Nepal, M. S. Onses, K. Park, M. Jespersen, C. J. Thode, P. F. Nealey, R. A. Vaia, *ACS Nano* **2012**, *6*, 5693.
- [29] A. Nemiroski, M. Gonidec, J. M. Fox, P. Jean-Remy, E. Turnage, G. M. Whitesides, *ACS Nano* **2014**, *8*, 11061.
- [30] E. S. A. Goerlitzer, R. Mohammadi, S. Nechayev, K. Volk, M. Rey, P. Banzer, M. Karg, N. Vogel, *Adv. Mater.* **2020**, *32*, 2001330.
- [31] Y. Brasse, V. Gupta, H. C. T. Schollbach, M. Karg, T. A. F. König, A. Fery, *Adv. Mater. Interfaces* **2020**, *7*, 1901678.
- [32] H. Lee, K. Song, M. Lee, J. Y. Park, *Adv. Sci.* **2020**, *7*, 2001148.
- [33] J. B. Lee, H. Walker, Y. Li, T. W. Nam, A. Rakovich, R. Sapienza, Y. S. Jung, Y. S. Nam, S. A. Maier, E. Corte, *ACS Nano* **2020**, *14*, 17693.
- [34] N. Pazos-Pérez, W. Ni, A. Schweikart, R. A. Alvarez-Puebla, A. Fery, L. M. Liz-Marzán, *Chem. Sci.* **2010**, *1*, 174.
- [35] M. Mayer, P. L. Potapov, D. Pohl, A. M. Steiner, J. Schultz, B. Rellinghaus, A. Lubk, T. A. F. König, A. Fery, *Nano Lett.* **2019**, *19*, 3854.
- [36] J. Langer, A. Mihi, C. Hanske, C. Matricardi, J. L. Garcia-Pomar, L. M. Liz-Marzán, *ACS Nano* **2018**, *12*, 8531.
- [37] G. Bodelón, V. Montes-García, V. López-Puente, E. H. Hill, C. Hamon, M. N. Sanz-Ortiz, S. Rodal-Cedeira, C. Costas, S. Celiksoy, I. Pérez-Juste, L. Scarabelli, A. La Porta, J. Pérez-Juste, I. Pastoriza-Santos, L. M. Liz-Marzán, *Nat. Mater.* **2016**, *15*, 1203.
- [38] C. Hanske, E. H. Hill, D. Vila-Liarte, G. González-Rubio, C. Matricardi, A. Mihi, L. M. Liz-Marzán, *ACS Appl. Mater. Interfaces* **2019**, *11*, 11763.
- [39] I.-K. Ding, J. Zhu, W. Cai, S.-J. Moon, N. Cai, P. Wang, S. M. Zakeeruddin, M. Grätzel, M. L. Brongersma, Y. Cui, M. D. McGehee, *Adv. Energy Mater.* **2011**, *1*, 52.
- [40] W. Li, Y. Zhou, I. R. Howell, Y. Gai, A. R. Naik, S. Li, K. R. Carter, J. J. Watkins, *ACS Appl. Mater. Interfaces* **2018**, *10*, 5447.
- [41] S. H. Ko, I. Park, H. Pan, C. P. Grigoropoulos, A. P. Pisano, C. K. Luscombe, J. M. J. Fréchet, *Nano Lett.* **2007**, *7*, 1869.
- [42] H. Agrawal, E. C. Garnett, *ACS Nano* **2020**, *14*, 11009.
- [43] S. Sarkar, V. Gupta, M. Kumar, J. Schubert, P. T. Probst, J. Joseph, T. A. F. König, *ACS Appl. Mater. Interfaces* **2019**, *11*, 13752.
- [44] S. Sarkar, V. Gupta, T. Tsuda, J. Gour, A. Singh, O. Aftenieva, A. M. Steiner, M. Hoffmann, S. Kumar, A. Fery, J. Joseph, T. A. F. König, *Adv. Funct. Mater.* **2021**, *31*, 2011099.
- [45] P. Probst, M. Mayer, V. Gupta, A. Steiner, Z. Zhou, G. Auernhammer, T. König, A. Fery, *Nat. Mater.* **2021**, <https://doi.org/10.1038/s41563-021-00991-8>.
- [46] L. E. Kreilkamp, V. I. Belotelov, J. Y. Chin, S. Neutzner, D. Dregely, T. Wehlus, I. A. Akimov, M. Bayer, B. Stritzker, H. Giessen, *Phys. Rev. X* **2014**, *3*, 041019.
- [47] P. Zeng, J. Cadusch, D. Chakraborty, T. A. Smith, A. Roberts, J. E. Sader, T. J. Davis, D. E. Gómez, *Nano Lett.* **2016**, *16*, 2651.
- [48] Y. Lee, J. Yun, S.-J. Kim, M. Seo, S. In, H.-D. Jeong, S.-Y. Lee, N. Park, T. D. Chung, B. Lee, *Adv. Opt. Mater.* **2020**, *8*, 2001256.
- [49] Y. Gao, W. Nie, Q. Zhu, X. Wang, S. Wang, F. Fan, C. Li, *Angew. Chem., Int. Ed.* **2020**, *59*, 18218.
- [50] C. Ng, J. J. Cadusch, S. Dligatch, A. Roberts, T. J. Davis, P. Mulvaney, D. E. Gómez, *ACS Nano* **2016**, *10*, 4704.
- [51] C. Ng, S. Dligatch, H. Amekura, T. J. Davis, D. E. Gómez, *Adv. Opt. Mater.* **2015**, *3*, 1582.
- [52] Q. Huang, T. D. Canady, R. Gupta, N. Li, S. Singamaneni, B. T. Cunningham, *ACS Photonics* **2020**, *7*, 1994.
- [53] Q.-Y. Lin, Z. Li, K. A. Brown, M. N. O'Brien, M. B. Ross, Y. Zhou, S. Butun, P.-C. Chen, G. C. Schatz, V. P. Dravid, K. Aydin, C. A. Mirkin, *Nano Lett.* **2015**, *15*, 4699.
- [54] Y. Hua, A. K. Fumani, T. W. Odom, *ACS Photonics* **2019**, *6*, 322.
- [55] A. M. Steiner, M. Mayer, M. Seuss, S. Nikolov, K. D. Harris, A. Alexeev, C. Kuttner, T. A. F. König, A. Fery, *ACS Nano* **2017**, *11*, 8871.
- [56] C. Hanske, M. Tebbe, C. Kuttner, V. Bieber, V. V. Tsukruk, M. Chanana, T. A. F. König, A. Fery, *Nano Lett.* **2014**, *14*, 6863.
- [57] S. Joseph, S. Sarkar, J. Joseph, *ACS Appl. Mater. Interfaces* **2020**, *12*, 46519.
- [58] K. Nagarajan, J. George, A. Thomas, E. Devaux, T. Chervy, S. Azzini, K. Joseph, A. Jouaiti, M. W. Hosseini, A. Kumar, C. Genet, N. Bartolo, C. Ciuti, T. W. Ebbesen, *ACS Nano* **2020**, *14*, 10219.
- [59] E. Orgiu, J. George, J. A. Hutchison, E. Devaux, J. F. Dayen, B. Doudin, F. Stellacci, C. Genet, J. Schachenmayer, C. Genes, G. Pupillo, P. Samorì, T. W. Ebbesen, *Nat. Mater.* **2015**, *14*, 1123.
- [60] Y. Yang, J. Wu, J. Li, *Appl. Phys. Lett.* **2016**, *109*, 91604.
- [61] M. L. Brongersma, N. J. Halas, P. Nordlander, *Nat. Nanotechnol.* **2015**, *10*, 25.
- [62] Z. Zhang, J. T. Yates, *Chem. Rev.* **2012**, *112*, 5520.
- [63] C. Lee, Y. K. Lee, Y. Park, J. Y. Park, *ACS Photonics* **2018**, *5*, 3499.
- [64] Y. Park, J. Choi, C. Lee, A. N. Cho, D. W. Cho, N. G. Park, H. Ihee, J. Y. Park, *Nano Lett.* **2019**, *19*, 5489.
- [65] J. B. Lee, H. Walker, Y. Li, T. W. Nam, A. Rakovich, R. Sapienza, Y. S. Jung, Y. S. Nam, S. A. Maier, E. Cortés, *ACS Nano* **2020**, *14*, 17693.
- [66] E. Dvininov, U. A. Joshi, J. R. Darwent, J. B. Claridge, Z. Xu, M. J. Rosseinsky, *Chem. Commun.* **2011**, *47*, 881.
- [67] L. Yu, J. Xi, M.-D. Li, H. T. Chan, T. Su, D. L. Phillips, W. K. Chan, *Phys. Chem. Chem. Phys.* **2012**, *14*, 3589.
- [68] X. Zhang, Y. L. Chen, R.-S. Liu, D. P. Tsai, *Rep. Prog. Phys.* **2013**, *76*, 46401.
- [69] M. Xiao, R. Jiang, F. Wang, C. Fang, J. Wang, C. Y. Jimmy, *J. Mater. Chem. A* **2013**, *1*, 5790.
- [70] S. S. E. Collins, E. K. Searles, L. J. Tauzin, M. Lou, L. Bursi, Y. Liu, J. Song, C. Flatebo, R. Baiyasi, Y. Cai, B. Foerster, T. Lian, P. Nordlander, S. Link, C. F. Landes, *ACS Nano* **2021**, *15*, 9522.
- [71] C. Shillingford, B. M. Kim, M. Weck, *ACS Nano* **2021**, *15*, 1640.
- [72] N. Sun, S.-T. Zhang, F. Simon, A. M. Steiner, J. Schubert, Y. Du, Z. Qiao, A. Fery, F. Lissel, *Angew. Chem., Int. Ed.* **2021**, *60*, 3912.
- [73] C. G. Tang, M. C. Y. Ang, K.-K. Choo, V. Keerthi, J.-K. Tan, M. N. Syafiqah, T. Kugler, J. H. Burroughes, R.-Q. Png, L.-L. Chua, P. K. H. Ho, *Nature* **2016**, *539*, 536.
- [74] A. K. Ghosh, S. Sarkar, L. J. Nebel, O. Aftenieva, V. Gupta, O. Sander, A. Das, J. Joseph, S. Wießner, T. A. F. König, A. Fery, *Adv. Funct. Mater.* **2021**, 2101959, <https://doi.org/10.1002/adfm.202101959>.
- [75] Lumerical Inc, <http://www.lumerical.com/tcad-products/fdtd/> (accessed: December 2020).
- [76] D. Smith; E. Shiles; M. Inokuti; E. Palik, *Handbook of Optical Constants of Solids*, Academic Press, Boston, MA **1985**, pp. 369–406.